Research article

An effective tellurium surface modification strategy to enhance the capacity and rate capability of Ni-rich $LiNi_{0.8}Co_{0.1}Mn_{0.1}O_2$ cathode material

Annam Butt [a],[1], Sidra Jamil [b],[**],[1], Muhammad Fasehullah [c], Haseeb Ahmad [e], Muhammad Khurram Tufail [d], Rehana Sharif [a], Ghulam Ali [e],[*]

[a] Department of Physics, University of Engineering and Technology, Lahore, 54890, Pakistan
[b] Laboratory of Luminescence Analysis and Molecular Sensing (Southwest University), Ministry of Education, School of Materials and Energy, Southwest University, Chongqing, 400715, PR China
[c] State Key Laboratory of Power Transmission Equipment & System Security and New Technology, Chongqing University, Chongqing, 400044, PR China
[d] College of Materials Science and Engineering, College of Physics, Qingdao University, Qingdao, 266071, PR China
[e] U.S.-Pakistan Center for Advanced Studies in Energy (USPCAS-E), National University of Science and Technology (NUST), Sector H-12, Islamabad, 44000, Pakistan

ARTICLE INFO

ABSTRACT

$LiNi_{0.8}Co_{0.1}Mn_{0.1}O_2$ (NCM) layered oxide is contemplated as an auspicious cathode candidate for commercialized lithium-ion batteries. Regardless, the successful commercial utilization of these materials is impeded by technical issues like structural degradation and poor cyclability. Elemental doping is among the most viable strategies for enhancing electrochemical performance. Herein, the preparation of surface tellurium-doped NCM is done by utilizing the methodology solid-state route at high temperatures. Surface doping of the Te ions leads to structural stability owing to the inactivation of oxygen at the surface via the binding of slabs of transition metal-oxygen. Remarkably, 1 wt% of Te doping in NCM exhibits enhanced electrochemical characteristics with an excellent discharge capacity, i.e., 225.8 mAh/g (0.1C), improved rate-capability of 156 mAh/g (5C) with 82.2% retention in capacity (0.5C) over 100 cycles within 2.7–4.3V as compared to all other prepared electrodes. Hence, the optimal doping of Te is favorable for enhancing capacity, cyclability along with rate capability of NCM.

1. Introduction

Lithium-ion batteries (LIBs) are treated as pervasive energy-storing technology for portable devices, automobile industry, and home appliances, attributed to high energy and power density, cost-effectiveness, long cyclic life, negligible memory loss, eco-friendliness, and low self-discharge [1–4]. However, further enhancement in the electrochemical performance is expeditiously required to fulfill the ever-growing demands for the system of energy storage on a commercial scale [5]. The cathode component of

LIBs is the most vital part of manufacturing electrochemically enhanced LIBs [6].

Ni-rich layered oxide (LiNi$_a$Co$_b$Mn$_c$O$_2$, a≥0.8, a+b + c = 1), wherein Ni composition is dominant over Mn and Co, are auspicious cathode candidates due to greater specific capacity, i.e., more than 200 mAh/g in 3.0–4.3 V, low cost, and exceptional energy density [7–9]. Unfortunately, the application of these materials still faces several challenges, including cation disorder and oxidation of Ni^{3+} to Ni^{4+} during cycling that can cause detrimental side reactions with electrolyte and formed Ni–O impurity phase [10–12]. Moreover, the conversion of R $\overline{3}$ m to Fd $\overline{3}$ m and then to Fm $\overline{3}$ m phase will give rise to anisotropic lattice contraction during the de-lithiation state that causes further structural degradation [13–15]. Hence, the abovementioned challenges should be resolved before the commercial-scale implementation of Ni-rich-based cathodes.

The electrochemical characteristics of these types of materials have been alleviated via several modification works, like doping, coating, pre-oxidation, and concentration gradient [16,17]. Among these modification strategies, element doping is the most feasible way to overcome structural instability and augment electrochemical stability [18–20]. To date, doping of the various elements, including Ti [21], Nb [22], Zr [23], Mo [24], V [25], Al [26], and so on, has been extensively examined to ameliorate electrochemical features.

The doping elements with dominantly stronger metal-oxygen bond energy can offer multiple advantages. Firstly, the dopant acts as a pillar by preventing the John-Teller distortion and ensures structural stability during cycling [27,28]. Secondly, cation disorder is prevented by restraining the evolution of oxygen [23,29]. In addition, the dopant with high bonding energy can also impede the reactivity between the electrode and electrolyte interface [10].

Moreover, dopants with high valence can be utilized to alleviate the electronic conductivity and mitigate polarization. Such metal ions present in transition metal slabs supply the additional charge and increase the force of repulsion among the layers. Consequently, the diffusivity of the Li$^+$ is increased by the increment of lattice and interlayer spacing. Hence, the cyclability, as well as rate capability, can be considerably ameliorated [25,30]. Furthermore, the dopants having large ionic radii compared with Ni, Mn, and Co can boost the rate capability by expanding the diffusion channels of Li$^+$ [26].

Various doping elements with high valence and bond dissociation energy have been explored. Li et al. [3] Nb-modified LiNi$_{0.8}$Co$_{0.1}$Mn$_{0.1}$O$_2$, the higher Nb and oxygen bond energy, less cation mixing, and expanded Li$^+$ diffusion paths lead to structural as well as cyclic stability. Park et al. [28] stated that B-doped LiNi$_{0.90}$Co$_{0.05}$Mn$_{0.05}$O$_2$ has 91% retention of capacity at 55 °C (100 cycles) by forming an optimized microstructure that can cause the slight release of internal strain during cycling. Jamil et al. [31] reported that Ta-doped LiNi$_{0.88}$Co$_{0.09}$Al$_{0.03}$O$_2$ exhibited enhanced rate capability and cyclability attributed to the robust Ta and oxygen bond dissociation energy. Shang et al. [32] illustrated that W-doped NCM811 at 4.5 V (100 cycles) exhibited 7.9% capacity loss, which was much lower than unmodified material owing to structural stability and lesser impedance value. Therefore, the utilization of Te^{6+} with high valence and 548 kJ/mol bond energy of Te–O [33] as a dopant in cathode materials can raise their electrochemical characteristics. Recently, Huang et al. [34] analyzed the impact of Te doping in LiNi$_{0.88}$Co$_{0.09}$Al$_{0.03}$O$_2$. The existence of a stronger bond between Te and oxygen inhibited the oxygen evolution and enhanced the phase reversibility (H2 → H3), which led to the stable structure along with the advancement in electrochemical characteristics.

In this study, Te-doped NCM cathodes were prepared using a two-step process involving hydroxide co-precipitation along with a solid-state technique with varying amounts of Te. This investigation focuses on a mechanistic perception of impact of tellurium doping on electrochemical characteristics of NCM.

2. Experimental details

2.1. Methodology

Hydroxide co-precipitation methodology was utilized to produce Ni$_{0.8}$Co$_{0.1}$Mn$_{0.1}$(OH)$_2$. Aqueous solutions (1 M) of NiSO$_4$·H$_2$O, MnSO$_4$·H$_2$O, and CoSO$_4$·6H$_2$O were pumped simultaneously with concentrated NaOH and NH$_3$. H$_2$O solution. Later on, 3 M NaOH was utilized to adjust pH. This mixture was vigorously stirred and kept at 50 °C, and hydroxide precursor was accumulated by filtration, washing, and then dried at 120 °C.

The LiNi$_{0.8}$Co$_{0.1}$Mn$_{0.1}$O$_2$ cathode material was obtained via hand grinding Ni$_{0.8}$Co$_{0.1}$Mn$_{0.1}$(OH)$_2$ with LiOH.H$_2$O (TM: Li = 1:1.03 mol ratio) using anhydrous ethanol (solvent) and finally pre-sintered (500 °C for 6 h) and after that sintered (750 °C for 20 h) in flowing oxygen environment marked as NCM.

The modified sample marked 1% Te-NCM was made via mixing the desired quantity of H$_6$TeO$_6$ in deionized water, then adding as-synthesized Ni$_{0.8}$Co$_{0.1}$Mn$_{0.1}$(OH)$_2$ in it so doping amount is 1 wt%. The excess water was removed by overnight heating at 80 °C. Then yield was blended with LiOH.H$_2$O and sintered under the same sintering conditions.

2.2. Material characterization

Structural investigation was conducted via X-ray diffraction (XRD) with Bruker D8 Advance instrument (λ = 0.158 nm). The microstructure was examined with high-resolution transmission electron microscopy (TEM) using G2 520 FEI, Tecnai instrument. Moreover, the element valence present on surface of as-prepared materials was examined via X-ray photoelectron spectroscopy (XPS) with ULVAC-PHI 5000 VersaProbe instrument via Al-K$_\alpha$ radiation hν = 1.4866 keV.

2.3. Electrochemical testing

To fabricate cathode, active material (80 %), conductive agent (10%), and binder (10%) were $LiNi_{0.8}Co_{0.1}Mn_{0.1}O_2$, conductive carbon, and polyvinylidene fluoride, respectively. *N*-methyl pyrrolidone (NMP) was taken as a solvent and slurry was pasted on an aluminum-foil sheet and subsequently vacuum-dried at 80 °C for overnight. Around 3 mg/cm^2 was the material loading on the cathode pellets. 1 M lithium hexafluorophosphate (LiPF$_6$) added in 1:1:1 vol % of EC/DMC/EMC mixture was utilized as an electrolyte. Li metal and Celgard 2325 (porous polypropylene S4 separator membrane) were taken as anode and separator, respectively. A glove box having pure argon was utilized to assemble CR2025 cells. To evaluate electrochemical performance at ambient temperature, coin cells were activated for four consecutive cycles (0.1C) and then continued at 0.5C and 2.7–4.3V for 100 cycles by a BST8 MTI battery tester.

3. Results and discussion

Structural investigation of NCM and Te-doped NCM materials via X-ray diffractometer (XRD) is demonstrated in Fig. 1 and Figure S1. The as-prepared samples display similar diffracted peaks that are associated with a hexagonal structure (α-NaFeO$_2$, R $\overline{3}$ m space group) (JCPDS #00-009-0063) and have no impurity peaks (Fig. 1(a) and Fig. S1 a) [35,36]. These results suggest that the Te addition did not vary the structure of NCM. Moreover, the magnified XRD graphs in the selected portion of 2θ (63–66°) (Fig. 1(b) and Fig. S1b) reveal that the peak splitting becomes less evident with the addition of Te. This may be associated with the conversion of phase near the surface of the materials [32,37]. Further analysis of the structural characteristics of pristine and Te-doped NCM is done by the Rietveld refinement method, and Fig. 1(c,d), Figure S1 (c,d), and Table 1 and table S1 present the corresponding outcomes. It can be perceived from profile refinements that the calculated curves are highly matched with the observed curves, and the R$_{wp}$ value for all the samples is <4%, which indicates the credibility of the refined data [3,38]. The c/a value is 4.9 for all the samples, which
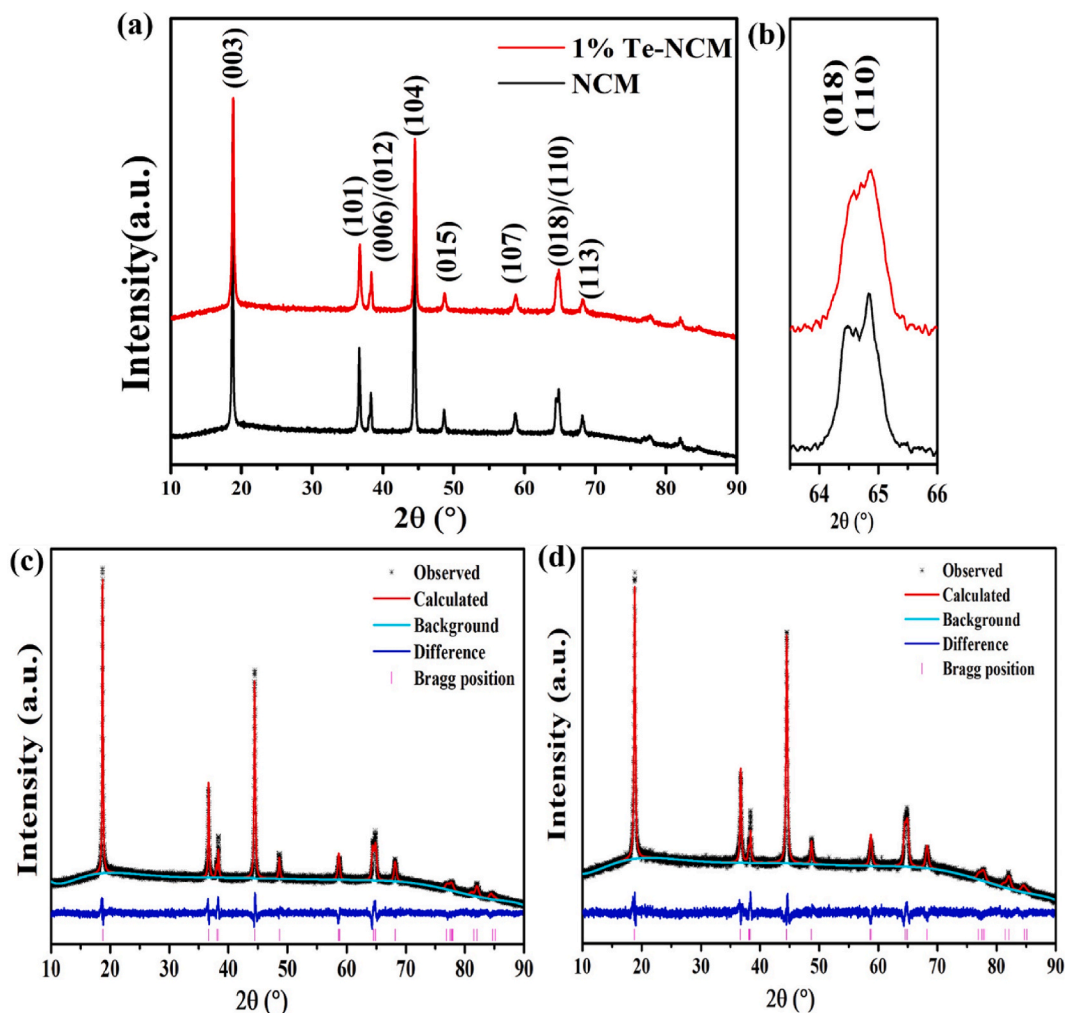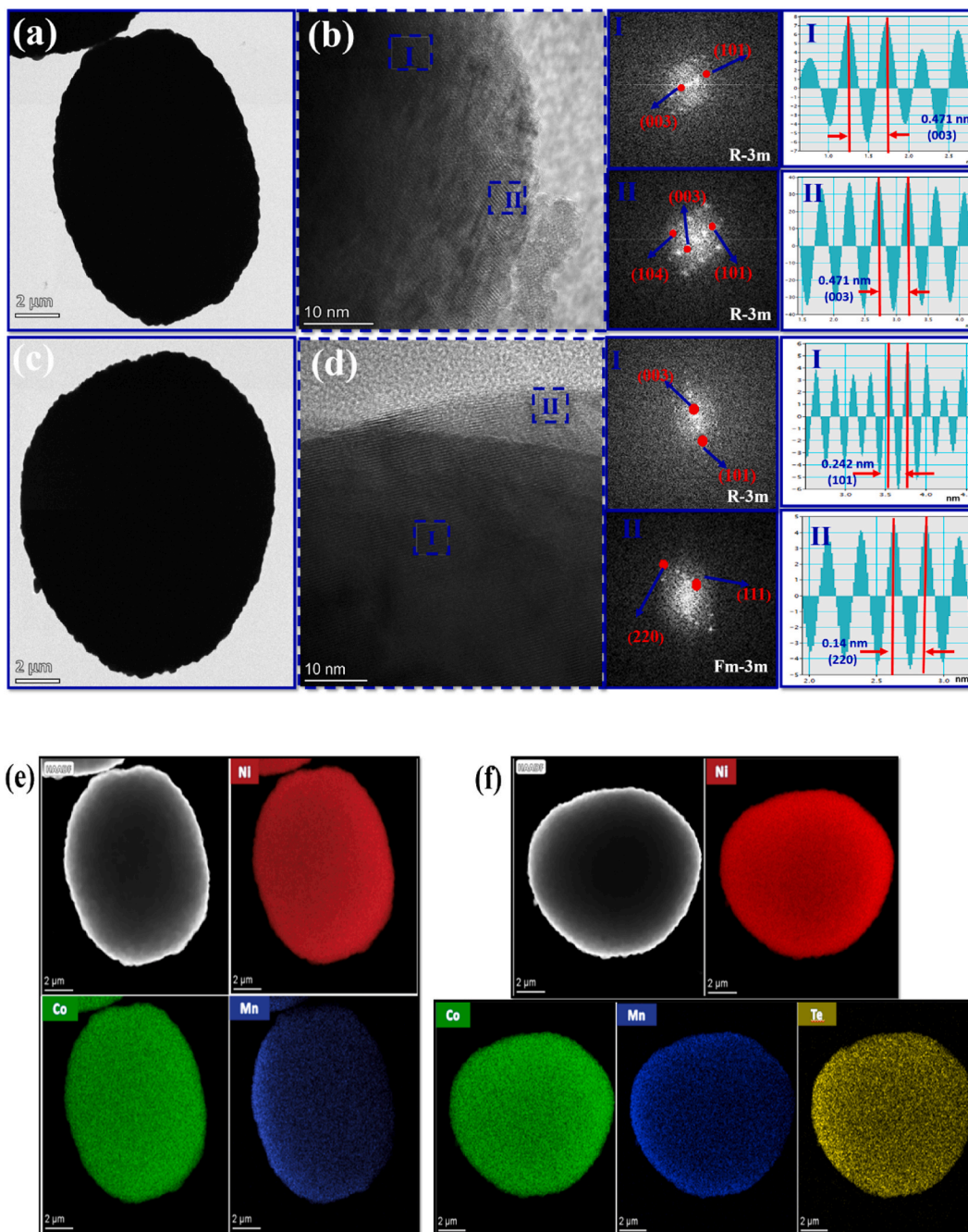

Fig. 1. (a) XRD profiles and (b) enlarged regions for (018)/(110) peaks and Rietveld-refinement of (c) NCM, and (d) 1% Te-NCM.

Table 1
Structural properties of NCM and Te-doped NCM from Rietveld refinement.

Sample	a (Å)	c (Å)	V(Å³)	c/a	$I_{(003)/(104)}$	R_{wp} (%)	Goodness of fit (GOF)
NCM	2.8743	14.212	101.687	4.94	1.38	3.32	1.46
1%Te-NCM	2.8745	14.215	101.714	4.94	1.19	3.07	1.38

Fig. 2. HRTEM images of (a) NCM (b) enlarge view as well as FFT images; (c) 1% Te-NCM (d) enlarge as well as FFT images; EDS mapping of Ni, Co, Mn of (e) NCM and EDS mapping of Ni, Co, Mn and Te of (f) 1% Te-NCM.

suggests that Te doping does not influence their well-ordered layered structure [16,31].

Furthermore, peak intensity ratio $R(I_{(003)/(104)})$ value is a crucial parameter in determining the structural order of cathode materials because (104) reflection does not depend on the disordering of structure. In comparison (003), reflection can be influenced by cation disorder in the layered structure [39,40]. A greater $R(I_{(003)/(104)})$ value suggests lower cation mixing [41,42]. Table 1 shows that doping of Te aggravates cation mixing, which can be explained based on charge conservation. The doping of Te^{6+} ions with a high valence state into layer of transition metal conserves charge by producing Ni^{2+}. Hence, the existence of more Ni^{2+} having similar ionic radii to Li^+, i.e., $r_{Ni}^{2+} = 0.69$ Å, $r_{Li}^+ = 0.72$ Å, facilitates the movement of Ni^{2+} into Li slab and promotes rock-salt phase at the surface [32, 37,43]. However, prior research has shown that a suitable quantity of rock-salt phase hinders the side reactions and enhances electrochemical performance [44,45].

The morphology and microstructural differences between Te-doped and pristine NCM are investigated through HRTEM. HRTEM
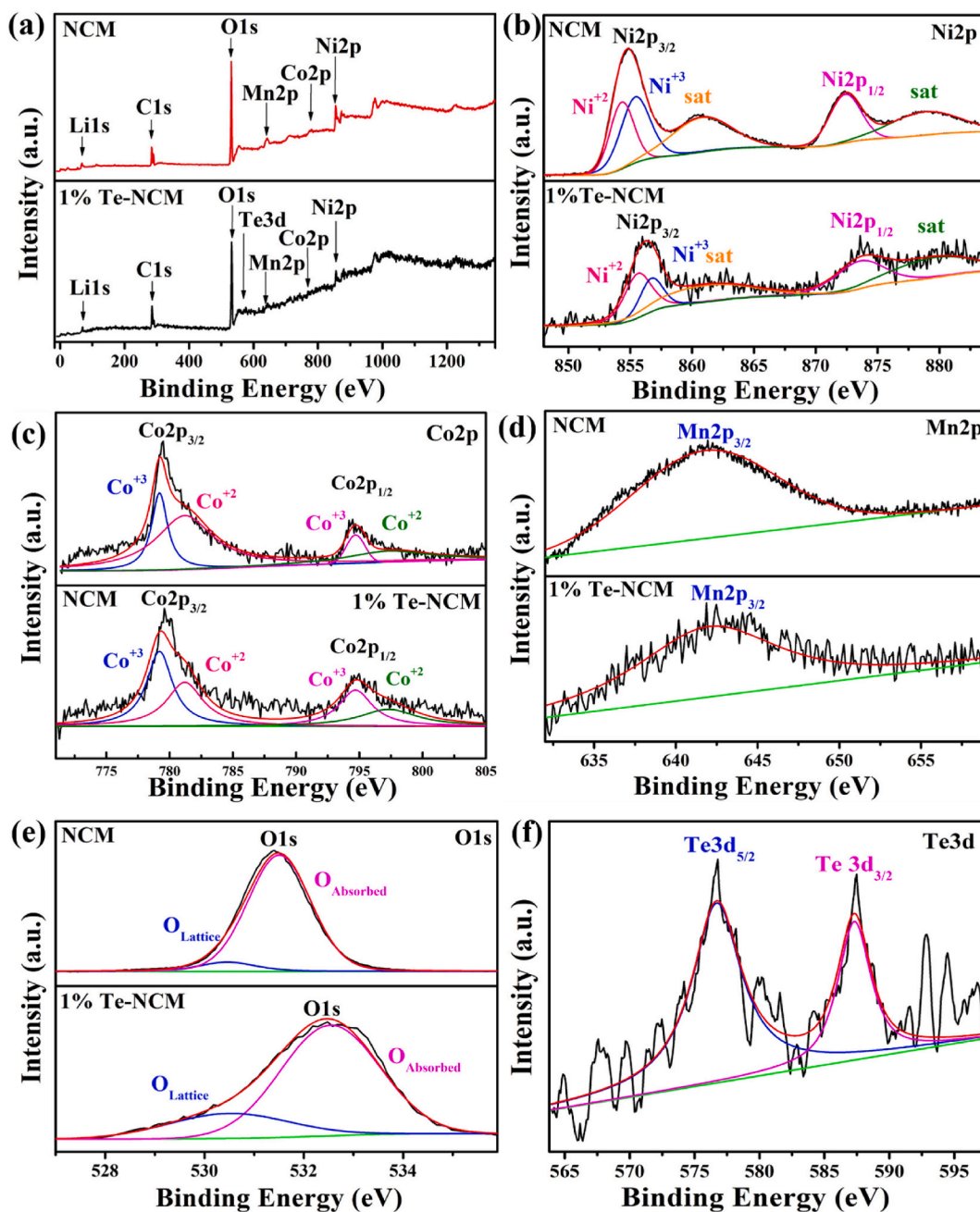
Fig. 3. XPS profiles (a) NCM and 1% Te NCM samples. Deconvoluted spectra (b) Ni 2p, (c) Co 2p, (d) Mn 2p, (e) O 1s, and (f) Te 3d for NCM and 1%NCM.

images with associated fast Fourier-transformation (FFT) patterns of pristine NCM, as well as 1% Te-NCM, are presented in Fig. 2 (a-d). Furthermore, Fig. 2(e and f) presents homogenous distribution of the elements in NCM and 1% Te-NCM. The HRTEM micrographs of both samples (Fig. 2 b,d) reveal a high crystalline nature represented by distinct fringes. The inter-atomic spacings in regions I & II of pristine NCM attribute to the (003) plane along with the adjacent (101) and (104) planes, manifest by FFT images, which confirms the existence of layered structure (R $\overline{3}$ m space group) [3,14,16]. However, 1% Te-doped NCM exhibits the layered structure in region I (bulk), while a rock salt phase (Fm $\overline{3}$ m) exists in region II (surface). The occurrence of Fm $\overline{3}$ m phase at surface, in conjunction with an increased Ni^{2+}/Ni^{3+} ratio (Fig. 1), indicates that the Te doping causes the creation of Fm $\overline{3}$ m phase on surface [24]. The rock-salt phase on the surface becomes active electrochemically to alleviate capacity, rate capability and retain the structural integrity of layered structure [35,41,46,47].

The investigation of the variation of the valence state of elements in NCM and 1% Te-NCM samples was done via XPS, as presented in Fig. 3. Binding energy peaks related to Li (1s), Co (2p), O (1s), Ni (2p), and Mn (2p) are observed for both samples, while a peak corresponding to Te (3d) is also detected in 1% Te-NCM (Fig. 3(a)). In Fig. 3(b), Ni 2p spectra of samples contain couple of prominent peaks that are associated with Ni $2p_{3/2}$ and Ni $2p_{1/2}$, together with satellite peaks. The deconvolution and fitting of peak Ni $2p_{3/2}$ reveal Ni^{2+} as well as Ni^{3+} existence on the surface. Ni $2p_{3/2}$ peak is found at 854.7 eV for NCM and 856.3 eV for 1% Te-NCM. So, after the Te doping, the Ni $2p_{3/2}$ peak moves from a lower to a greater value of binding energy, implying the likely rise of Ni^{2+} near the surface to conserve the charge according to the previous reports of doping of high oxidation state metal ions [32,48].

Moreover, it can be observed from spectra that Ni^{2+}/Ni^{3+} is greater for 1% Te-NCM as compared to NCM. Hence, also in accordance with XRD results, it could be deduced that the enrichment of Te ion close to the surface results in the conversion of Ni^{3+} into Ni^{2+} and originates cation mixing [32,48,49]. However, more Ni^{2+} produces a rock-salt phase on surface that may enhance structural stability [50]. The peaks in Co 2p spectra of both samples belong to Co $2p_{3/2}$, as well as Co $2p_{1/2}$, as illustrated in Fig. 3(c). The diversion of Co $2p_{3/2}$ peak to the elevated binding energy after Te doping may be attributed to Co^{3+} to Co^{2+} ion adjustment to retain the charge equilibrium [34]. In Mn 2p spectra (Fig. 3(d)), the Mn $2p_{3/2}$ is positioned at 641.8 eV and 642 eV for NCM and 1% Te-NCM corresponding to Mn^{4+} [51]. Moreover, in O 1s spectra, as displayed in Fig. 3(e), two peaks belong to lattice oxygen (Mn/Co–O bonds) and absorbed oxygen (LiOH and Li_2CO_3). Peak intensity of the lattice oxygen increases after Te doping, implying that the strong Te–O bonds produce more lattice oxygen and enhance structural stability [31]. As illustrated in Fig. 3(f), peaks positioned at 576.3 and 587.3 eV are linked with Te $3d_{5/2}$ and Te $3d_{3/2}$, accordingly, revealing that valence state of Te is +6 [34].

The electrochemical characteristics of NCM and 1% Te-NCM cathodes are demonstrated in Fig. 4(a-d). Fig. 4(a) presents 1st cycle voltage curves within 2.7 and 4.3 V (0.1C). NCM and 1% Te-NCM discharge capacity are 188.4 and 225.8 mAh/g, correspodingly. Increased discharge capacity is ascribed to appropriate doping of Te on the surface because, during discharging, Li ions can go back to
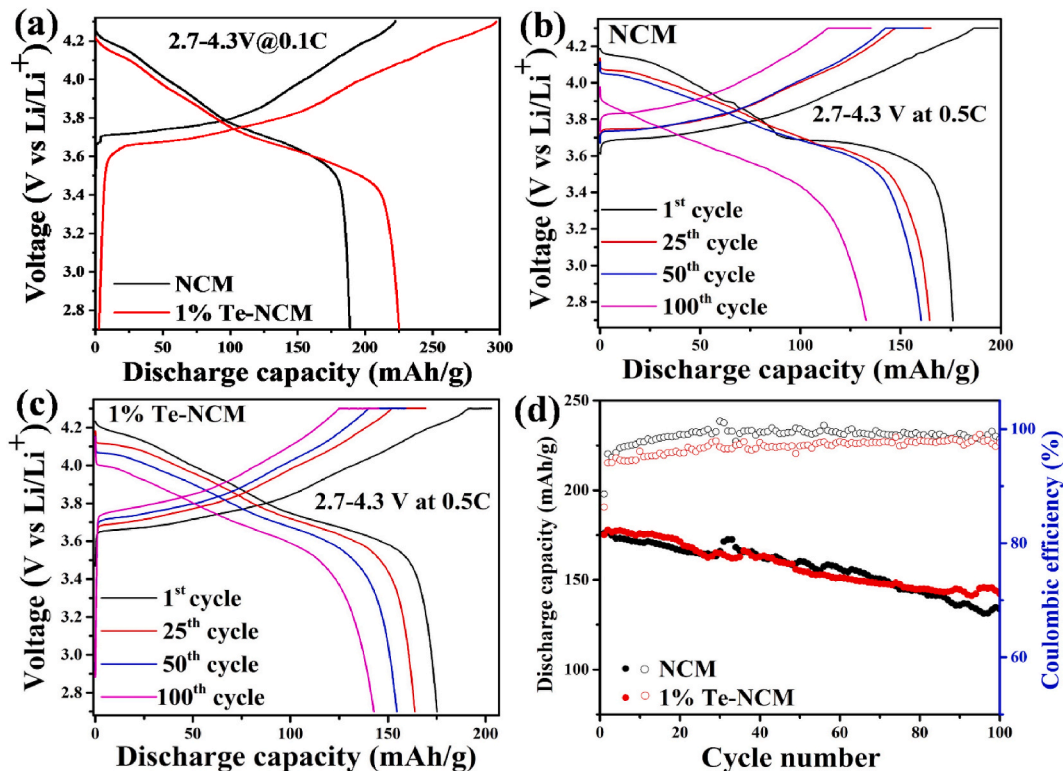

Fig. 4. (a) Initial cycling graphs of NCM and 1% Te-NCM (0.1C, 2.7–4.3 V). Charge-discharge graphs (b) NCM (c) 1% Te-NCM (0.5C, 2.7–4.3 V) at 1st, 25th, 50th, and 100th cycle. (d) Cyclic stability of pristine NCM and 1% Te-NCM between 2.7 and 4.3 V (0.5C, 100 cycles).

their respective positions without cation mixing. Furthermore, cycling curves of NCM and 1% Te-NCM at 0.5C between a potential of 2.7–4.3 V are depicted in Fig. 4(b-c). Observably, an preliminary potential drops during discharge and a voltage plateau throughout cycling are evident which are accredited to the impedance of the cells. The NCM has a potential drop of 0.15 V which is very less than 0.33 V of 1% Te-NCM after 100 cycles. Moreover, electrochemical features of NCM with 1% Te-NCM is further compared by calculating the discharge plateau retention (DPR) using the formula in Eq. (1) [52]:

$$DPR = \frac{PC}{DC} \tag{1}$$

Where the PC and DC are discharge capacities from preliminary discharge potential to potential of 3.5 and 2.7 V, respectively. The DPR of 1% Te-NCM is 80.1% which is far higher than 66.7% of NCM at the 100th cycle.

The NCM cathode has variations in charge/discharge curves (Fig. 4(b and c)) at extended cycles owing to the polarization of the electrode, which is due to structural degradation. However, 1% Te-NCM maintains similar profiles, a small potential drop, and has a slower capacity decay due to the strong Te–O bonding that can effectively reduce degradation of structure [34]. Fig. 4(d) illustrates cyclic behavior of NCM and 1% Te-NCM at 0.5C. 1% Te-NCM has 82.2% retention in the capacity which is higher than 74.6% of NCM over 100 cycles. Enhanced cyclability of 1% Te-NCM can be accredited to the surface doping of tellurium ions and the inactivation of oxygen at the surface by binding the slabs of TM-O through the presence of strong bonding between the Te ions and oxygen that facilitates the structural stability upon cycling [34].

Fig. 5(a-b) depicts cyclic voltammetry (CV) profiles at 0.1 mV/s and 2.7–4.3 V. NCM as well as 1% Te-NCM electrodes have three cathodic and anodic peaks, related to transition of phase from (i) hexagonal (H1) to monoclinic (M) phase (3.7–3.9 V), (ii) monoclinic (M) to hexagonal structure (H2) (3.9–4.1 V) and (iii) hexagonal (H2) to hexagonal (H3) phase during Li-ions insertion/extraction. In the process of phase transformation from H2 → H3, the more extraction of the lithium ions will contract the c parameter, and expedite a large variation volume as well as micro stress [53]. As a result, layered structure will collapse and degrade cyclability of material [54]. Fig. 5 indicates the smaller H3 peak of 1% Te-NCM compared to NCM, which infers the restraining effect of Te on the occurrence of the H3 phase and, as a result, the enhancement of structural stability. In addition, the overlapping of CV curves is better for 1% Te-NCM than NCM, which indicates better reversibility [55].

At several C-rates from 0.1 to 5C after every four-cycle and then restored to 0.1C, rate capability of NCM, and 1% Te-NCM cathode materials are demonstrated in Fig. 6(a). Both samples have a decreasing trend of capacity with the increment in the C-rate, which is caused by polarization. Furthermore, the specific capacities of the 1% Te-NCM sample have superior values in comparison with NCM. It can also be observed from the results that the 1% Te-NCM still offers ~156 mAh/g (5C), which is considerably greater than pristine NCM (~123.1 mAh/g). Also, when C-rate is restored to 0.1C, 1% Te-NCM still provides a capacity of 212.3 mAh/g, over NCM (193.2 mAh/g). Hence, 1% Te-NCM cathode attains greater capacity and enhanced rate capability owing to its structural retention after the migration of Li-ions.

The interfacial characteristic of both prepared samples was investigated after the 3rd and 100th cycles via electrochemical impedance spectroscopy (EIS) along with the Nyquist curves depicted in Fig. 6(b). The region of high-frequency provides insight into surface film resistance (R_s) as well as charge transfer resistance (R_{ct}) present at interfacial region. On the other hand, region of low frequency is ascribed to Warburg impedance which gives valuable information about Li^+ diffusion kinetics [56,57].

The resistance values in Table 2 depict a harsh increase in surface film along with R_{ct} of NCM from 32.29 to 100.5 Ω for the 3rd to 100th cycle, respectively. Whereas 1% Te-NCM represents a slight increment in $R_{sf} + R_{ct}$ from 17.24 to 40.87 Ω. The lower impedance values indicate decline of side reactions that occur among cathode and electrolyte along with the facilitation of Li^+ diffusivity. The Li^+ diffusion coefficient is listed in Table 2, evaluated via equation (1):
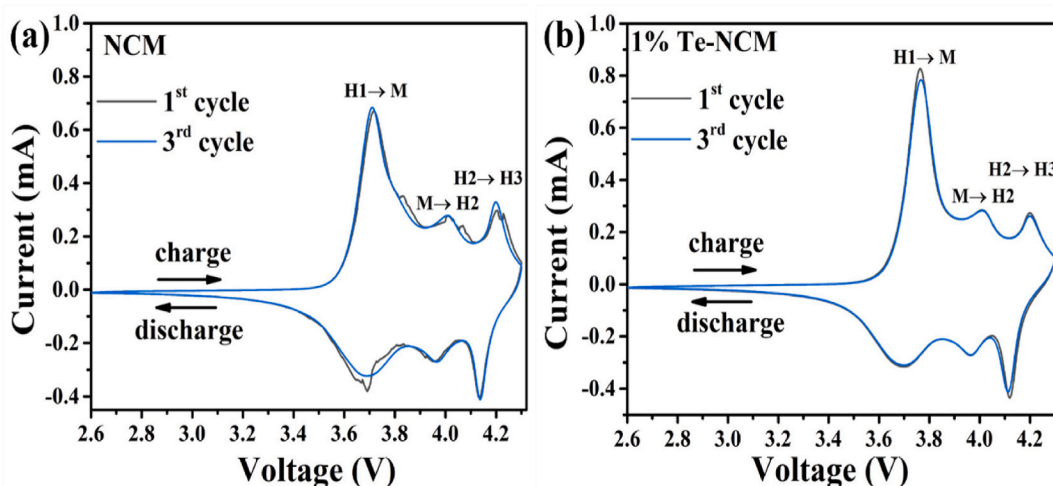

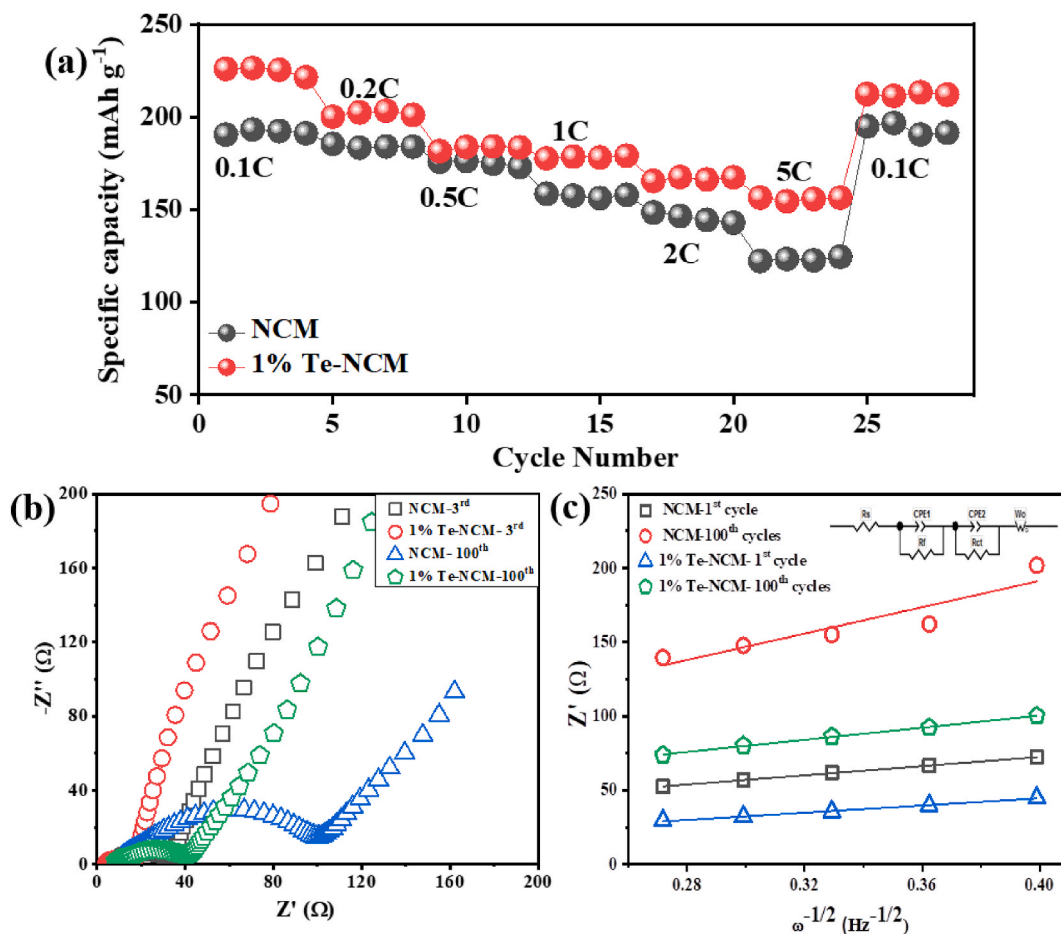**Fig. 5.** The CV profile (a) NCM (b) 1% Te-NCM (0.1 mV/s, 2.7–4.3 V).

Fig. 6. (a) Rate capability (b) Nyquist plots of NCM and 1% Te-NCM cathodes (c) plots of Z′ versus $\omega^{-1/2}$.

Table 2
EIS fitted values after 3rd and 100th cycles with corresponding lithium-ion diffusion coefficient.

Samples	3rd Cycle		100th Cycle	
	$R_{sf} + R_{ct}(\Omega)$	$D_{Li+}(cm^2/S)$	$R_{sf} + R_{ct}(\Omega)$	$D_{Li+}(cm^2/S)$
NCM	32.29	2.55×10^{-12}	100.5	2.43×10^{-13}
1% Te-NCM	17.24	4.57×10^{-12}	40.87	1.32×10^{-12}

$$D_{Li^+} = \frac{R^2 T^2}{2A^2 n^4 F^4 C^2 \sigma^2} \tag{1b}$$

Here R is gas constant, n denotes the number of electrons for lithium ions, A stands for geometric area i.e., 0.785 cm^2 of the electrode, T stands for the kelvin temperature, F denotes Faraday's constant and C is lithium ions' concentration *i.e.* 0.001 mol/cm^3 and also σ (Warburg impedance) is determined by equation (2):

$$Z' = R_{sf} + R_{ct} + \sigma \omega^{-1/2} \tag{2}$$

For NCM, calculated Li$^+$ diffusion coefficients are 2.55×10^{-12} and 2.43×10^{-13} cm^2/S after tested for 3rd and 100th cycles respectively. In comparison for 1% Te-NCM, D_{Li^+} are 4.57×10^{-12}, and 1.37×10^{-12} cm^2/S after tested for 3rd and 100th cycles respectively. Hence, 1% Te-NCM exhibits enhanced Li$^+$ transportation and stabilized cathode-electrolyte interface. A comparison of the electrochemical characteristics of NCM after doping with various elements is shown in Table 3.

Table 3
Comparitive electrochemical performance of NCM after doping with various elements.

Doping element	Potential	Discharge capacity (mAh/g)	Retention/Cycle Number	Reference
Ti	2.8–4.3	214.9 at 0.1C	77%/150/1C	[58]
Nb	3.0–4.3	202.3 at 0.1C	90.6%/100/0.1C	[59]
Zr	3.0–4.5	180 at 1C	74%/200/1C	[60]
Te	**2.7–4.3**	**225.8 at 0.1 C**	**82.2%/100/0.5C**	**This work**

4. Conclusion

In summary, pristine NCM and Te surface-doped NCM cathode materials are prepared via a solid-state route at high temperatures. The optimal Te doping (1 wt %) boosted electrochemical features of cathode material. The presence of strong bonding between Te and oxygen becomes the cause of binding the TM-O slabs and prevents the surface oxygen emission and consequently reduces the structural degradation. Specifically, 1% Te-NCM provides a higher capacity of 225.8 mAh/g (0.1C) and 156 mAh/g (5C), as compared to pristine NCM (188.4 mAh/g (0.1C), and 123.1 mAh/g (5C)). Furthermore, retention of capacity for 1% Te-NCM and NCM are 82.2% and 74.6% respectively at 0.5C over 100 cycles. Hence, 1% Te-NCM with remarkable capacity, improved rate capability, along with excellent cyclability, can be a promising LIB cathode.

Data availability statement

No data was used for the research described in the article.

CRediT authorship contribution statement

Annam Butt: Writing – original draft, Investigation, Conceptualization. **Sidra Jamil:** Writing – original draft, Formal analysis, Data curation. **Muhammad Fasehullah:** Investigation, Formal analysis. **Haseeb Ahmad:** Project administration, Investigation. **Muhammad Khurram Tufail:** Investigation, Conceptualization. **Rehana Sharif:** Validation, Supervision. **Ghulam Ali:** Writing – review & editing, Validation, Supervision, Funding acquisition.

Declaration of competing interest

The authors declare that they have no known competing financial interests or personal relationships that could have appeared to influence the work reported in this paper.

Appendix ASupplementary data

Supplementary data to this article can be found online at https://doi.org/10.1016/j.heliyon.2024.e28039.

References

[1] X. Wang, et al., Ni-Rich/Co-Poor layered cathode for automotive Li-ion batteries: promises and challenges, Adv. Energy Mater. 10 (12) (2020) 1903864.
[2] J. Zheng, et al., Effect of calcination temperature on the electrochemical properties of nickel-rich LiNi0. 76Mn0. 14Co0. 10O2 cathodes for lithium-ion batteries, Nano Energy 49 (2018) 538–548.
[3] J. Li, et al., An effective doping strategy to improve the cyclic stability and rate capability of Ni-rich LiNi0. 8Co0. 1Mn0. 1O2 cathode, Chem. Eng. J. 402 (2020) 126195.
[4] S. Jamil, et al., Challenges and prospects of nickel-rich layered oxide cathode material, J. Alloys Compd. 909 (2022) 164727.
[5] Y. Liu, et al., Enhancement on structural stability of Ni-rich cathode materials by in-situ fabricating dual-modified layer for lithium-ion batteries, Nano Energy 65 (2019) 104043.
[6] L. Yao, et al., Improved electrochemical property of Ni-rich LiNi0. 6Co0. 2Mn0. 2O2 cathode via in-situ ZrO2 coating for high energy density lithium ion batteries, Chem. Eng. J. 389 (2020) 124403.
[7] Z. Feng, et al., In-situ formation of hybrid Li3PO4-AlPO4-Al (PO3) 3 coating layer on LiNi0. 8Co0. 1Mn0. 1O2 cathode with enhanced electrochemical properties for lithium-ion battery, Chem. Eng. J. 382 (2020) 122959.
[8] R. Qian, et al., Enhanced surface chemical and structural stability of Ni-rich cathode materials by synchronous lithium-ion conductor coating for lithium-ion batteries, ACS Appl. Mater. Interfaces 12 (12) (2020) 13813–13823.
[9] A. Butt, et al., Elevated Li+ diffusivity in Ni-rich layered oxide by precursor pre-oxidation, Ceram. Int. 48 (20) (2022) 30176–30183.
[10] M. Jeong, et al., Stabilizing effects of Al-doping on Ni-rich LiNi0. 80Co0. 15Mn0. 05O2 cathode for Li rechargeable batteries, J. Power Sources 474 (2020) 228592.

[11] A. Butt, et al., Recent advances in enhanced performance of Ni-rich cathode materials for Li-ion batteries: a review, Energy Technol. 10 (3) (2022) 2100775.
[12] S. Jamil, et al., Improved high-voltage performance of LiNi0.87Co0.1Al0.03O2 by Li+-conductor coating, Chem. Eng. J. 407 (2021) 126442.
[13] H. Yang, et al., Simultaneously dual modification of Ni-rich layered oxide cathode for high-energy lithium-ion batteries, Adv. Funct. Mater. 29 (13) (2019) 1808825.
[14] L. Wu, et al., Improvement of electrochemical reversibility of the Ni-Rich cathode material by gallium doping, J. Power Sources 445 (2020) 227337.
[15] S.S. Zhang, Problems and their origins of Ni-rich layered oxide cathode materials, Energy Storage Mater. 24 (2020) 247–254.
[16] Y.-C. Li, et al., Synergy of doping and coating induced heterogeneous structure and concentration gradient in Ni-rich cathode for enhanced electrochemical performance, J. Power Sources 423 (2019) 144–151.
[17] Y. Tang, et al., Synergistic role of Sb doping and surface modification in high performance ultrahigh-nickel layered oxides cathode materials, J. Alloys Compd. 959 (2023) 170552.
[18] W. Mo, et al., Tuning the surface of LiNi0. 8Co0. 1Mn0. 1O2 primary particle with lithium boron oxide toward stable cycling, Chem. Eng. J. 400 (2020) 125820.
[19] S. Jamil, et al., Suppressing H2–H3 phase transition in high Ni–low Co layered oxide cathode material by dual modification, J. Mater. Chem. A 8 (40) (2020) 21306–21316.
[20] Y. Zhou, et al., Relieving stress concentration through anion–cation codoping toward highly stable nickel-rich cathode, ACS Nano 17 (20) (2023) 20621–20633.
[21] J. Li, et al., A facile method to enhance electrochemical performance of high-nickel cathode material Li (Ni 0.8 Co 0.1 Mn 0.1) O 2 via Ti doping, J. Mater. Sci. Mater. Electron. 29 (13) (2018) 10702–10708.
[22] Z. Zhao, et al., Cation mixing effect regulation by niobium for high voltage single-crystalline nickel-rich cathodes, Chem. Eng. J. 461 (2023) 142093.
[23] X. Li, et al., Dual functions of zirconium modification on improving the electrochemical performance of Ni-rich LiNi 0.8 Co 0.1 Mn 0.1 O 2, Sustain. Energy Fuels 2 (2) (2018) 413–421.
[24] Y. Su, et al., Improving the cycling stability of Ni-rich cathode materials by fabricating surface rock salt phase, Electrochim. Acta 292 (2018) 217–226.
[25] S.-J. Sim, et al., Improving the electrochemical performances using a V-doped Ni-rich NCM cathode, Sci. Rep. 9 (1) (2019) 1–8.
[26] X. Zhang, C. Liu, Z. Rao, Experimental investigation on thermal management performance of electric vehicle power battery using composite phase change material, J. Clean. Prod. 201 (2018) 916–924.
[27] F. Schipper, et al., Stabilizing nickel-rich layered cathode materials by a high-charge cation doping strategy: zirconium-doped LiNi 0.6 Co 0.2 Mn 0.2 O 2, J. Mater. Chem. A 4 (41) (2016) 16073–16084.
[28] K.J. Park, et al., Improved cycling stability of Li [Ni0. 90Co0. 05Mn0. 05] O2 through microstructure modification by boron doping for Li-ion batteries, Adv. Energy Mater. 8 (25) (2018) 1801202.
[29] M. Eilers-Rethwisch, M. Winter, F.M. Schappacher, Synthesis, electrochemical investigation and structural analysis of doped Li [Ni0. 6Mn0. 2Co0. 2-xMx] O2 (x= 0, 0.05; M= Al, Fe, Sn) cathode materials, J. Power Sources 387 (2018) 101–107.
[30] Y. Zhang, et al., Studies on stability and capacity for long-life cycle performance of Li (Ni0. 5Co0. 2Mn0. 3) O2 by Mo modification for lithium-ion battery, J. Power Sources 358 (2017) 1–12.
[31] Y. Huang, et al., Improving the structure and cycling stability of Ni-rich layered cathodes by dual modification of yttrium doping and surface coating, ACS Appl. Mater. Interfaces 12 (17) (2020) 19483–19494.
[32] G. Shang, et al., Enhancing structural stability unto 4.5 V of Ni-rich cathodes by tungsten-doping for lithium storage, J. Power Sources 423 (2019) 246–254.
[33] J. Meng, et al., Enhanced structural stability and improved electrochemical performance of layered lithium-rich cathode materials via tellurium doping, J. Electrochem. Soc. 164 (12) (2017) A2594.
[34] Y. Huang, et al., Tellurium surface doping to enhance the structural stability and electrochemical performance of layered Ni-rich cathodes, ACS Appl. Mater. Interfaces 11 (43) (2019) 40022–40033.
[35] S. Jamil, et al., Significantly fastened redox kinetics in single crystal layered oxide cathode by gradient doping, Nano Energy 94 (2022) 106961.
[36] B. Chu, et al., Enhancing the cycling stability of Ni-rich LiNi0. 6Co0. 2Mn0. 2O2 cathode at a high cutoff voltage with Ta doping, ACS Sustain. Chem. Eng. 8 (8) (2020) 3082–3090.
[37] G.-T. Park, et al., Tungsten doping for stabilization of Li [Ni0. 90Co0. 05Mn0. 05] O2 cathode for Li-ion battery at high voltage, J. Power Sources 442 (2019) 227242.
[38] W. Ge, L. Bai, X. Li, Effects of reheating temperature on the structure, morphology and electrochemical performance of Ni-rich cathode materials, J. Alloys Compd. 876 (2021) 160098.
[39] H. Jia, et al., Precursor effects on structural ordering and electrochemical performances of Ni-rich layered LiNi0. 8Co0. 2O2 cathode materials for high-rate lithium ion batteries, Electrochim. Acta 266 (2018) 7–16.
[40] X. Qu, et al., An integrated surface coating strategy to enhance the electrochemical performance of nickel-rich layered cathodes, Nano Energy 91 (2022) 106665.
[41] S. Jamil, et al., Ni/Li antisite induced disordered passivation layer for high-Ni layered oxide cathode material, Energy Storage Mater. 45 (2022) 720–729.
[42] Y.-C. Li, et al., Construction of homogeneously Al3+ doped Ni rich Ni-Co-Mn cathode with high stable cycling performance and storage stability via scalable continuous precipitation, Electrochim. Acta 291 (2018) 84–94.
[43] H.-H. Ryu, et al., Suppressing detrimental phase transitions via tungsten doping of LiNiO 2 cathode for next-generation lithium-ion batteries, J. Mater. Chem. A 7 (31) (2019) 18580–18588.
[44] U.-H. Kim, et al., Pushing the limit of layered transition metal oxide cathodes for high-energy density rechargeable Li ion batteries, Energy Environ. Sci. 11 (5) (2018) 1271–1279.
[45] T. He, et al., Sufficient utilization of Zr4+ on improving the structure and surface property of the Ni-rich cathode materials for lithium ion batteries, ChemSusChem 11 (2018) 1639–1648.
[46] Z. Ding, et al., Stable heteroepitaxial interface of Li-rich layered oxide cathodes with enhanced lithium storage, Energy Storage Mater. 21 (2019) 69–76.
[47] W. Li, et al., Regulating the grain orientation and surface structure of primary particles through tungsten modification to comprehensively enhance the performance of nickel-rich cathode materials, ACS Appl. Mater. Interfaces 12 (42) (2020) 47513–47525.
[48] C. Xu, et al., Highly stabilized Ni-rich cathode material with Mo induced epitaxially grown nanostructured hybrid surface for high-performance lithium-ion batteries, ACS Appl. Mater. Interfaces 11 (18) (2019) 16629–16638.
[49] Y. Cho, P. Oh, J. Cho, A new type of protective surface layer for high-capacity Ni-based cathode materials: nanoscaled surface pillaring layer, Nano Lett. 13 (3) (2013) 1145–1152.
[50] L. Liu, et al., Layered ternary metal oxides: performance degradation mechanisms as cathodes, and design strategies for high-performance batteries, Prog. Mater. Sci. (2020) 100655.
[51] M. Zhang, et al., Yttrium modified Ni-rich LiNi0. 8Co0. 1Mn0. 1O2 with enhanced electrochemical performance as high energy density cathode material at 4.5 V high voltage, J. Alloys Compd. 774 (2019) 82–92.
[52] Y. Chen, et al., Enhancing the high-voltage electrochemical performance of the LiNi 0.5 Co 0.2 Mn 0.3 O 2 cathode materials via hydrothermal lithiation, J. Mater. Sci. 53 (2018) 2115–2126.
[53] S. Jamil, et al., Dual cationic modified high Ni-low co layered oxide cathode with a heteroepitaxial interface for high energy-density lithium-ion batteries, Chem. Eng. J. 416 (2021) 129118.
[54] F. Zhu, et al., Enhanced electrochemical performance of LiNi0. 8Co0. 1Mn0. 1O2 via titanium and boron co-doping, Ceram. Int. 47 (3) (2021) 3070–3078.
[55] H. Liu, et al., Fast potassium migration in mesoporous carbon with ultrathin framework boosting superior rate performance for high-power potassium storage, Energy Storage Mater. 40 (2021) 490–498.
[56] S. Jamil, et al., Significance of gallium doping for high Ni, low Co/Mn layered oxide cathode material, Chem. Eng. J. 441 (2022) 135821.
[57] B. Cao, et al., MOF-derived ZnS nanodots/Ti 3 C 2 T x MXene hybrids boosting superior lithium storage performance, Nano-Micro Lett. 13 (2021) 1–17.

[58] D. Zhang, et al., Effect of Ti ion doping on electrochemical performance of Ni-rich LiNi0. 8Co0. 1Mn0. 1O2 cathode material, Electrochim. Acta 328 (2019) 135086.

[59] Y.-R. Kim, et al., Effect of niobium doping to enhance electrochemical performances of LiNi0. 8Co0. 1Mn0. 1O2 cathode material, Solid State Ionics 389 (2023) 116108.

[60] K. Wu, et al., Revealing the multiple influences of Zr substitution on the structural and electrochemical behavior of high nickel LiNi0. 8Co0. 1Mn0. 1O2 cathode material, J. Phys. Chem. C 125 (19) (2021) 10260–10273.